Electronic Supplementary Material (ESI) for Catalysis Science & Technology.

Supporting Information for

Electrocatalytic Hydrogen Production from Neutral Water Using an Aqueous Ni(II) Pincer Complex

Somayeh Norouziyanlakvan, Jonathan Ferguson, Darrin Richeson

EXPERIMENTAL:

General:

Reagents and analytical grade solvents were purchased from Strem Chemicals or Sigma Aldrich and used without further purification.

X-ray Crystallography: The crystal of (**1**) was mounted on thin glass fibers using paraffin oil. Prior to data collection crystals were cooled to 200.15 °K. Data were collected on a Bruker Smart ApexII single crystal diffractometer equipped with a sealed tube Mo source (wavelength 0.71073 Å) and an ApexII CCD detector. Raw data collection and processing were performed with the Apex3 software package from Bruker.[2] Initial unit cell parameters were determined from 60 data frames from select ω scans collected at the different sections of the Ewald sphere. Semi-empirical absorption corrections based on equivalent reflections were applied.[3] Systematic absences in the diffraction data-set and unit-cell parameters were consistent with the assigned space group. The initial structural solution was determined using ShelxT direct methods,[4] and refined with full-matrix least-squares procedures based on F^2 using ShelXle.[5] Hydrogen atoms were placed geometrically and refined using a riding model. All scattering factors are contained in several versions of the ShelXL program library, with the latest version used being v.6.12 at the time of this writing.[4]

Electrochemistry: Electrochemical experiments were carried out in a single compartment cells, with 50 mL approximate volumes, using a VersaSTAT 3 (Princeton Applied Research) potentiostat. Samples were prepared in open air, sealed, and connected to a Schlenk line and maintained under a nitrogen atmosphere. A conventional three electrode system was employed consisting of a glassy carbon working electrode (diameter = 0.3 cm), a Pt wire or a GC rod was used as the auxiliary electrode, and an Ag/AgCl reference electrode. 0.3M aqueous Phosphate buffer with pH=7 was used as solvent using deionized water. Aqueous measurements were also made replacing the Pt counter electrode with a GC electrode. Dry potassium bromide (KBr), the supporting electrolytes, was purchased from Sigma. For the experiments in acetonitrile, dry MeCN was used as solvent with Bu_4NPF_6 as supporting electrolyte and TFA as proton source. In these reactions silver wire was used as pseudo-reference electrode and ferrocene was added as an internal reference. The potential of the pseudo-reference was checked against ferrocene before and after each experiment. The typical concentration of catalyst was 1 mM in each experiment.

Other Physical Measurements:

Gas chromatography (GC) for detection of H_2 was conducted on a Shimadzu GC- 2014 equipped with a thermal conductivity detector (TCD). Helium carrier gas (purity ≥ 99.995%) was utilized with an isothermal 6-minute run at 30 ºC on an Agilent HP-PLOT Q column. UV-vis spectra were recorded with a Cary 100 spectrophotometer. The ^1H and $^{13}C\{^1H\}$ NMR spectra were recorded at 600 MHz respectively with chemical shifts reported in ppm using the residual protons of the NMR solvent as internal standards. Mass spectrometric measurements were performed at the Chemistry Mass Spectrometry Facility at the University of Ottawa, Ontario on a Micromass Quattro triple quadrapole mass spectrometer equipped with an electrospray ionization source.

Calculations:

For experiments in aqueous solutions, Turnover frequency, Faradaic efficiency, and overpotential were calculated using equations in below:

TOF (mol H_2/mol catalyst·h) = (charge from catalyst solution during CPE – charge from solution without catalyst during CPE) / (Faraday's constant × mol of electrons required to generate a mol of H_2 /mol of catalyst in solution × duration of electrolysis in hours)

Faradaic yield (%) = (mol of H_2 produced × mol of electrons needed to generate a mol of H_2 × 100) / mol of electrons supplied by electron source.

Overpotential = |applied potential– E(pH of solution at the end of the electrolysis)|.

Synthesis of 2,6-bis[(1-phenylimino)ethyl]pyridine:

Aniline (5 mL, 55 mmol) was added to a solution of 2,6-diacetylpyridine (0.489 g, 3 mmol) in absolute propan-2-ol (50 mL). The reaction mixture was refluxed for 2 h and then allowed to cool to room temperature. The crude product precipitated as a yellow powder. Pure product was obtained in 90% yield upon recrystallization from methanol. 1H NMR (60 MHz, CDCl3); δ 8.32 (m, py, 3 H), 7.1 (m, Ph, 10 H), and 2.41 (s, CH3, 6 H) ppm.

Table S1. Crystal data and structure refinement for **(1)**

Compound	
Empirical formula	$C_{21}H_{19}Br_2NiN_3$
Formula weight	531
Temperature(K)	203(2)
λ (Å)	0.71073
Crystal system	Monoclinic
Space group	C 2/c
a (Å)	15.9809(5)
b (Å)	8.5994(3)
c (Å)	15.5441(5)
α (deg)	90.00
β (deg)	102.998(1)
γ (deg)	90.00
V (Å3)	2081.43(12)
Z	4
DX (calc) (g/cm^3)	1.697
Mu (mm-1)	4.782
R1a	0.0244
wR2b	0.0650

Table S2. Selected Bond lengths [Å] and angles [°] for (**1**).

Bond lengths [Å]		**Bond angles [°]**	
Br(1)-Ni(1)	2.3967	N(1)-Ni(1)-N(2)	78.1
Ni(1)-N(1)	1.947	Br(1)-Ni(1)-N(1)	112.41
Ni(1)-N(2)	2.114	Br(1)-Ni(1)-N(2)	96.40
N(1)-C(3)	1.338	Br(1)-Ni(1)-Br(2)	135.18
N(2)-C(4)	1.278(4)	Ni(1)-N(1)-C(3)	118.8
N(2)-C(6)	1.436(4)	Ni(1)-N(2)-C(4)	114.7
C(1)-C(2)	1.381	Ni(1)-N(2)-C(6)	123.7
C(2)-C(3)	1.388(4)	C(4)-N(2)-C(6)	121.5(3)
C(4)-C(5)	1.491(5)	C(3)-C(4)-C(5)	119.8(3)

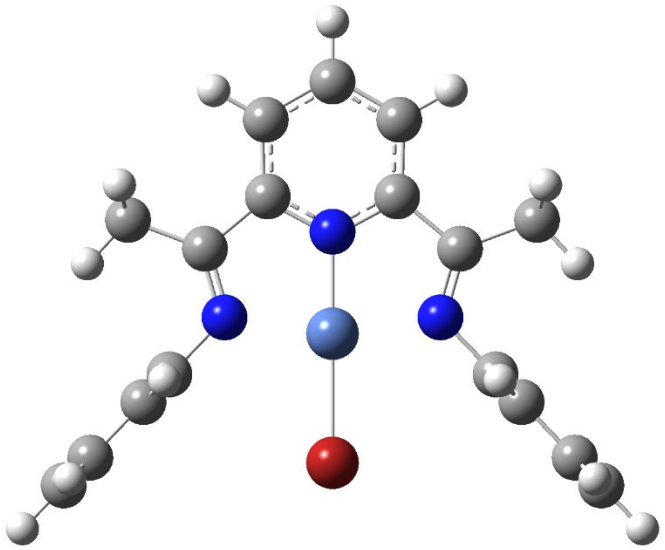

Figure S1. Computationally optimized [Ni(κ^3-2,6-{PhNCMe}$_2$(NC_5H_3)Br]$^+$ (**1'$^+$**) (DFT, B3LYP, def2-TZVP) using the PCM model for solvation in acetonitrile.

Table S3. Selected bonding parameters for computationally optimized [Ni(κ^3-2,6-{PhNCMe}$_2$(NC_5H_3)Br]$^+$ (**1'$^+$**)

Bond	Length(Å)	Overlap Pop	Mayer Bond Order
Ni-N_{py}	1.847	0.2092273	0.6811206
Ni-N_{imine}	1.976	0.2650285	0.6542685
Ni-Br	2.339	0.3438040	1.0047678

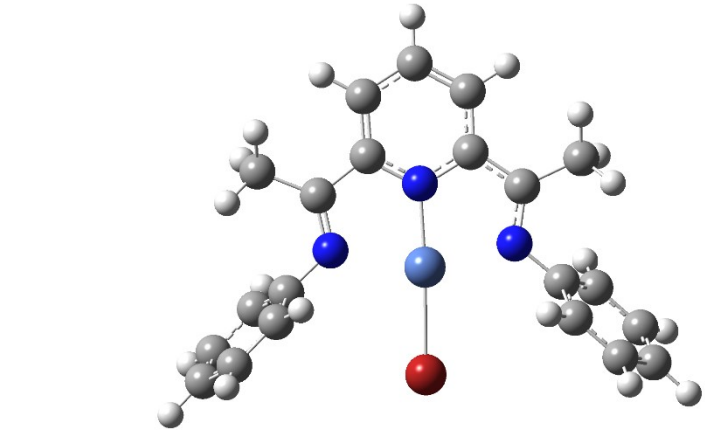

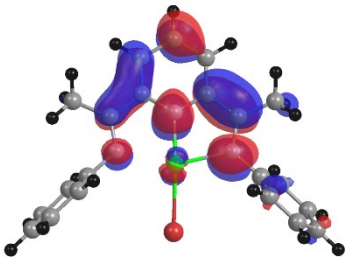

MO116 SOMO

0.48 py, 0.40 imine

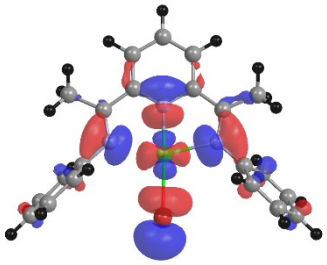

MO115 SOMO

0.41 Ni x^2-y^2, 0.19 Br p_y

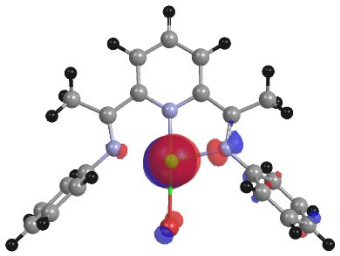

MO112 0.73 (Ni) 0.15 (Br)

Figure S2. Computationally optimized [Ni(κ^3-2,6-{PhNCMe}$_2$(NC_5H_3)Br]$^-$ (**1'$^-$**) Both the singlet and triplet states of were successfully optimized to confirmed minima and the triplet state was determined to be lower in energy than the singlet state by 9 kcal/mole. Representations and fragment allocation of the two singly occupied molecular orbitals (SOMO) and a dz^2 localized lone electron pair (MO112) for the DFT optimized [Ni(κ^3-2,6-{PhNCMe}$_2$(NC_5H_3)Br]$^-$ (**1'$^-$**) in the triplet state (DFT, B3LYP, def2-TZVP) using the PCM model for solvation in acetonitrile. The orbitals are rendered using the Chemissian software with an isosurface of 0.03.

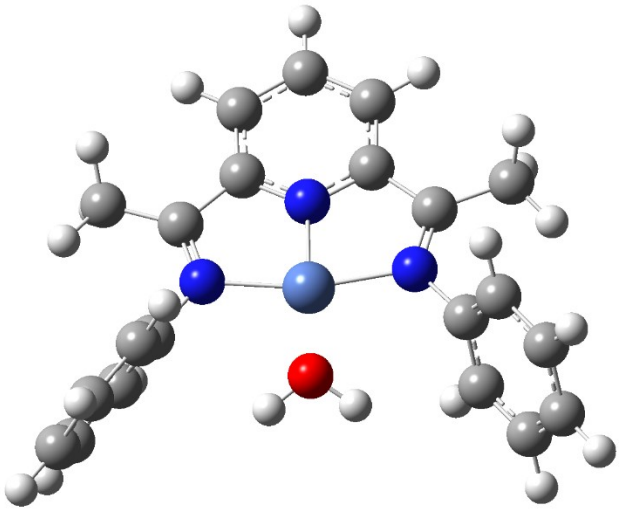

Figures S3. Computationally optimized $[Ni(\kappa^3\text{-}2,6\text{-}\{PhNCMe\}_2(NC_5H_3)(OH_2)]^{2+}$ (**1'(OH$_2$)$^{2+}$**) (DFT, B3LYP, def2-TZVP, PCM in water).

Table S4. Selected bond parameters for computationally optimized $[Ni(\kappa^3\text{-}2,6\text{-}\{PhNCMe\}_2NC_5H_3)(OH_2)]^{2+}$ (**1'(OH$_2$)$^{2+}$**)

bond	Length(Å)	Mayer Bond order
Ni-N_{py}	1.820	0.7364718
Ni-N_{imine}	1.948	0.6848865
Ni-N_{imine}	1.947	0.6879363
Ni-O	1.932	0.3857002

Table S5. Selected bond parameters for computationally optimized $[Ni(\kappa^3\text{-}2,6\text{-}\{PhNCMe\}_2NC_5H_3)(OH_2)]$ (**1'(OH$_2$)**). The product of the second reduction of **1'(OH$_2$)$^{2+}$**).

Bond	Length(Å)	Mayer Bond order
Ni-N_{py}	1.913	0.6058021
Ni-N_{imine}	2.087	0.4681138
Ni-N_{imine}	2.127	0.4131332
Ni-O	2.101	0.2051176

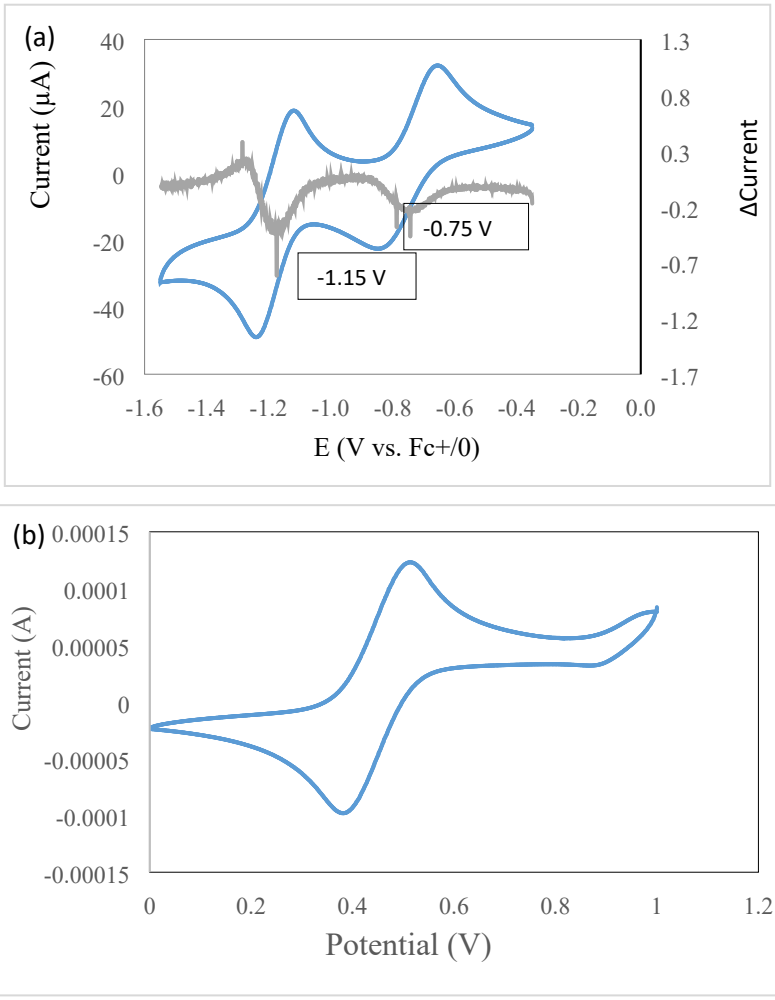

Figure S4. (a) Cyclic voltammogram of $[Ni(\kappa^3\text{-}2,6\text{-}\{PhNCMe\}_2(NC_5H_3)Br]^+$ (**1'**$^+$) (1mM) in CH_3CN with 100mM $TBAPF_6$ using a glassy carbon (GC) working electrode. Potentials are referenced to Fc/Fc^+. A quasireversible and reversible reduction peaks were observed with $E_{1/2}$ of -0.75 V and -1.15 V, respectively. The gray markers represent application of the method of first principles to the blue curve. Minima denote inflection points in the catalytic curve and indicate the associated onset potential and current enhancement. (b) Cyclic voltammogram of ferrocene (1mM) as a reference in CH_3CN with 100mM $TBAPF_6$ using a glassy carbon (GC) working electrode. The ΔE_p value was 131mV.

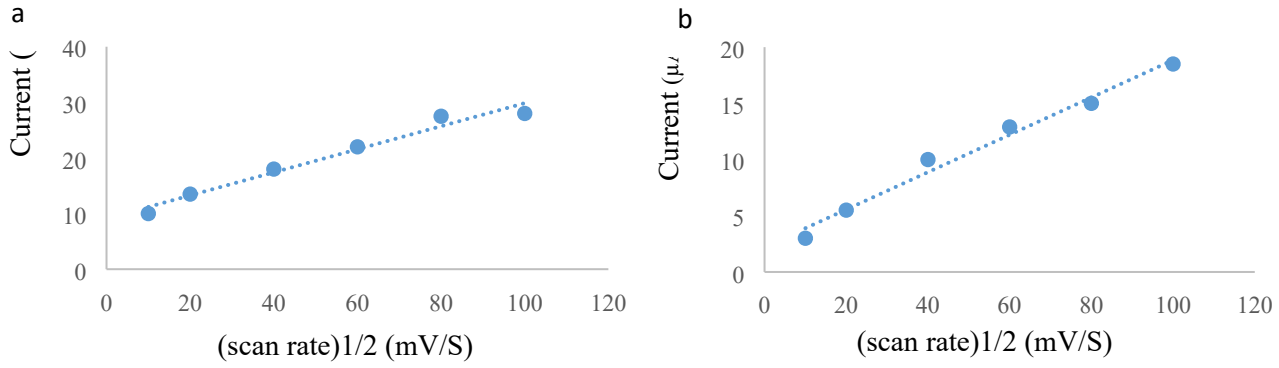

Figure S5. Plots of scan rate$^{1/2}$ versus current for the (a) first at -0.8V, (b) second at -1.2 V, reduction peaks of (**1'**$^{+}$).

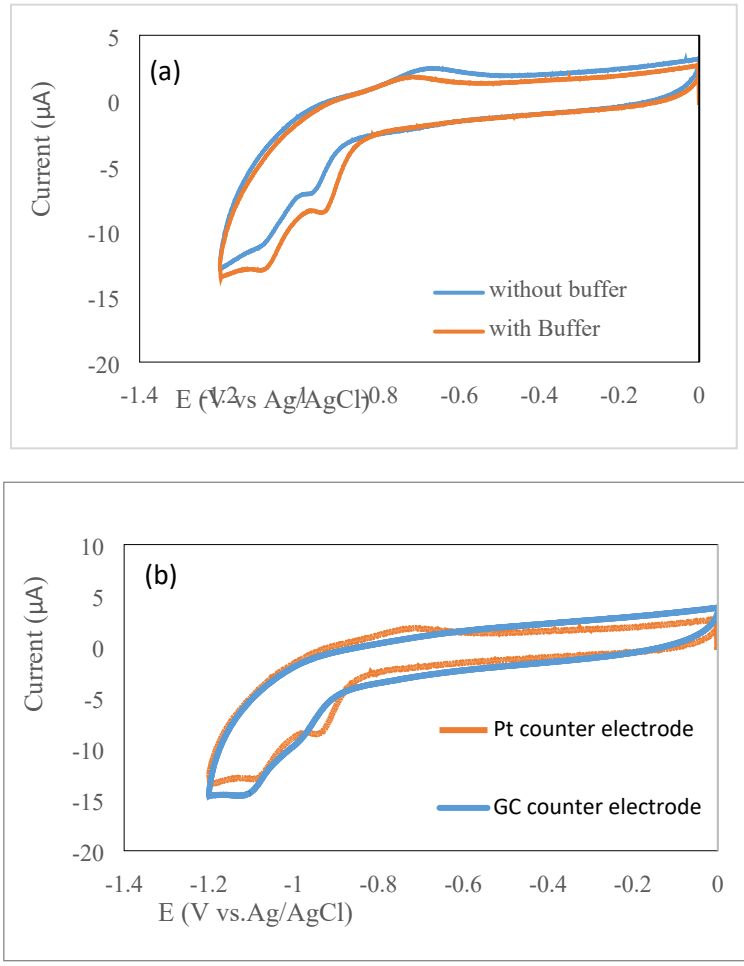

Figure S6. Cyclic voltammogram of complex $[Ni(\kappa^3\text{-}2,6\text{-}\{PhNCMe\}_2(NC_5H_3)(OH_2)]^{2+}$ (**1'$(OH_2)^{2+}$**) (1mM) in presence of 100mM KBr in H_2O using a glassy carbon (GC) working electrode, Ag/AgCl reference electrode. (a) Using a Pt counter electrode with (orange) and without (blue) 0.3M phosphate buffer pH=7. (b) Comparison of using Pt or GC counter electrode under the same conditions.

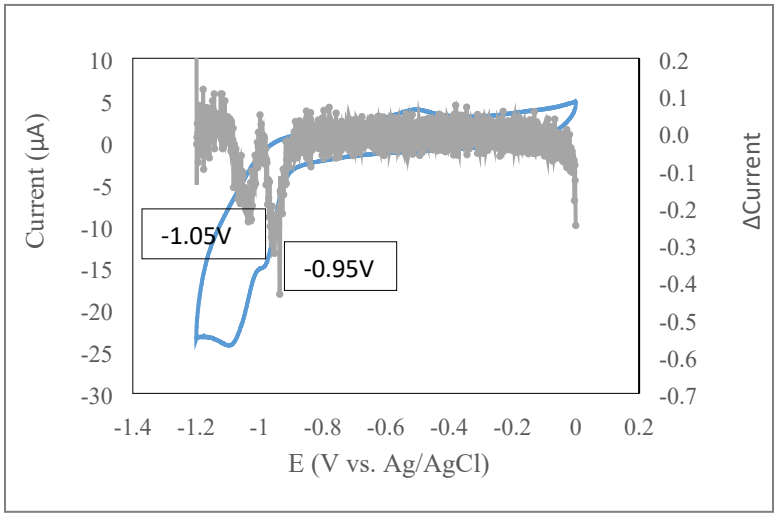

Figure S7. Cyclic voltammogram of complex $[Ni(\kappa^3\text{-}2,6\text{-}\{PhNCMe\}_2(NC_5H_3)(OH_2)]^{2+}$ (**1'$(OH_2)^{2+}$**) (1mM) in presence of 100mM KBr in phosphate buffer pH=7, using a glassy carbon (GC) working electrode, Ag/AgCl reference electrode. Two irreversible reduction peaks and an oxidation peak were observed with $E_{1/2}$ of -0.95 V and -1.05 V, and -0.5 V versus Ag/AgCl. The gray markers represent application of the method of first principles to the blue curve. Minima denote inflection points in the catalytic curve and indicate the associated onset potential and current enhancement.

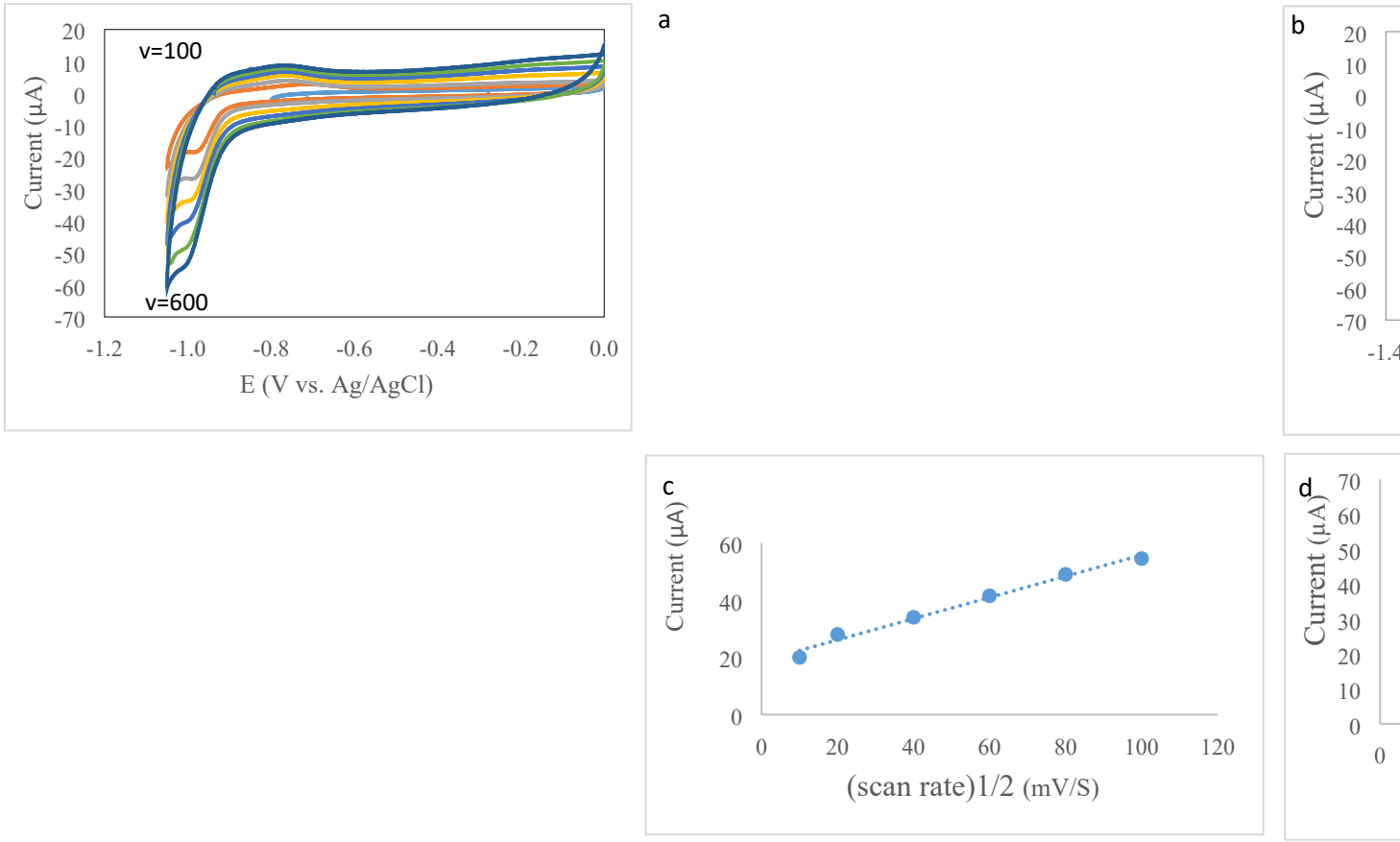

Figure S8. Cyclic voltammogram of complex $[Ni(\kappa^3\text{-}2,6\text{-}\{PhNCMe\}_2(NC_5H_3)(OH_2)]^{2+}$ (**1'(OH$_2$)$^{2+}$**) (1mM) at different scan rates in presence of 0.1M KBr in 0.3M phosphate buffer pH=7 for a) the first reduction, b) the first and the second reductions. Plots of scan rate$^{1/2}$ versus current for the first reduction (c) and the second reduction (d) at half wave potential. All potentials are referenced to Ag/AgCl.

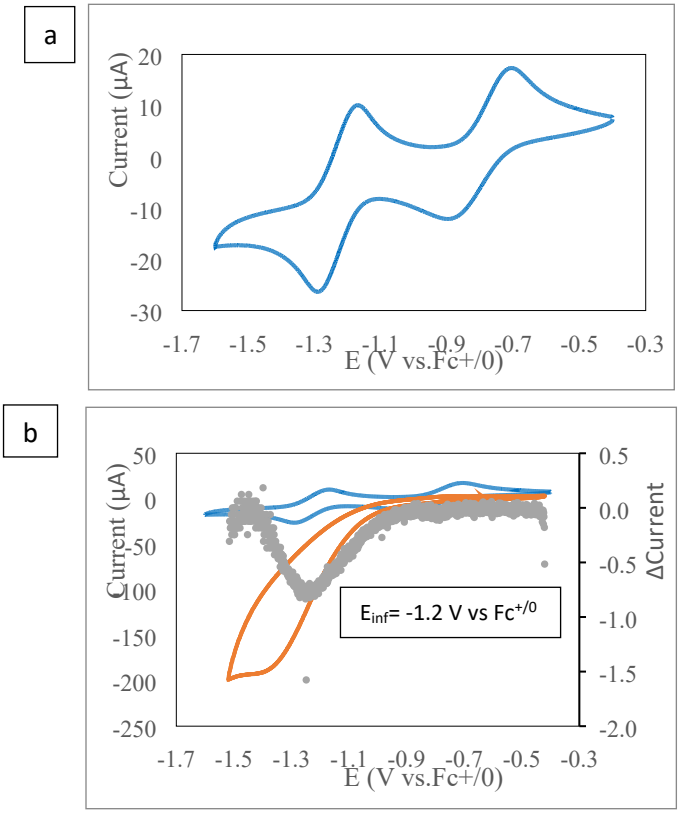

Figure S9. (a) Cyclic voltammogram of complex [Ni(κ^3-2,6-{PhNCMe}$_2$(NC$_5$H$_3$)Br]$^+$ (**1'$^+$**) (1mM) in CH$_3$CN with 100mM TBAPF$_6$ using a glassy carbon (GC) working electrode. b) Cyclic voltammograms of complex [Ni(κ^3-2,6-{PhNCMe}$_2$(NC$_5$H$_3$)Br]$^+$ (**1'$^+$**) (1mM) in CH$_3$CN in the absence (blue) and presence (orange) of trifluoroacetic acid (TFA). The gray markers represent application of the method of first principles to the orange curve. Minima denote inflection points in the catalytic curve and indicate the associated onset potential and current enhancement.

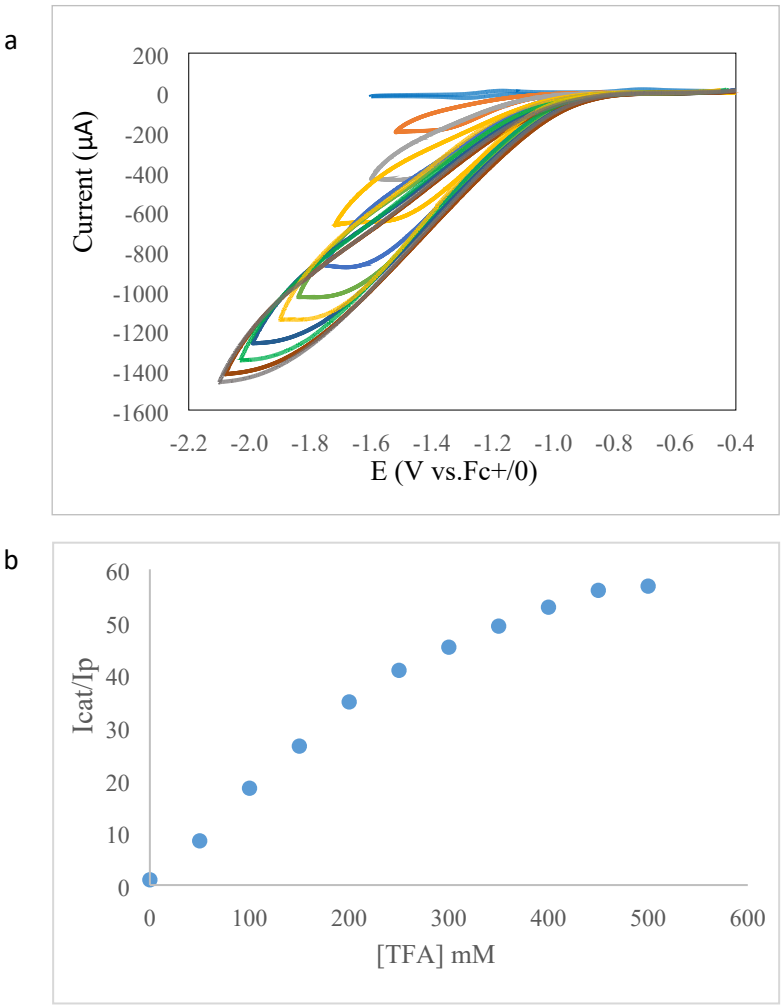

Figure S10. a) Cyclic voltammograms of $[Ni(\kappa^3\text{-}2,6\text{-}\{PhNCMe\}_2(NC_5H_3)Br]^+$ **(1'⁺)** in the absence of TFA and with varying concentrations of TFA in CH_3CN with 0.1 M tetrabutylammonium hexafluorophosphate ($TBAPF_6$) supporting electrolyte at 100 mV/s using a glassy carbon (GC) working electrode. (b) Corresponding plot of i_{cat}/i_p vs TFA concentration.

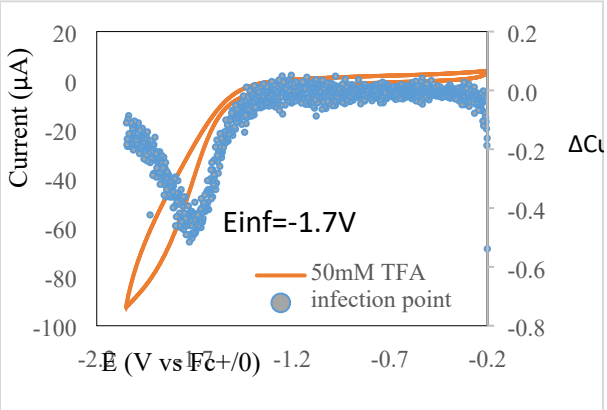

Figure S11. Background cyclic voltammogram showing current enhancements related to the reduction of the TFA by the GC electrode. Solution contained 0.1M $TBAPF_6$ and 50mM TFA. The CV was performed at a scan rate of 100mV/s. The blue markers represent application of the method of first principles to the orange curve. Minima denote inflection points in the catalytic curve and indicate the associated onset potential and current enhancement.

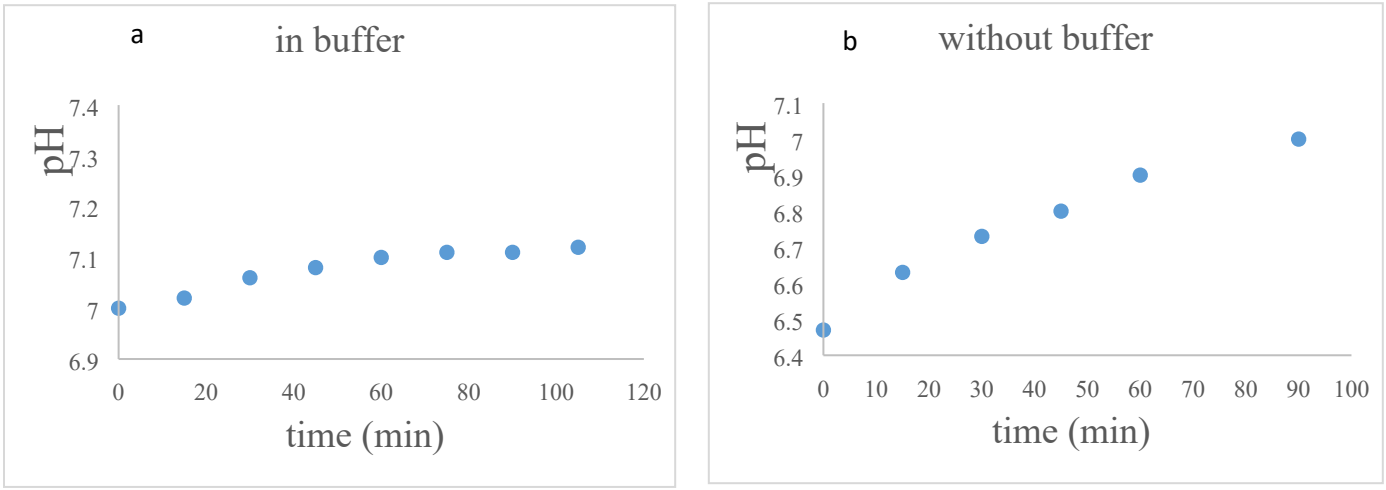

Figure S12. Plot of pH change during electrolysis a) in presence phosphate buffer pH 7 b) absence of buffer. Both Solutions containe 1mM **1'$(OH_2)^{2+}$** and 0.1 M KBr in aqueous solution and the CPE was done at –1.2 V vs. Ag/AgCl.

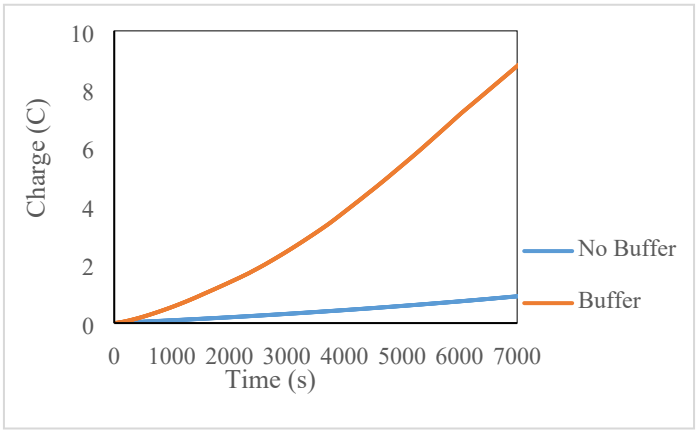

Figure S13. Controlled potential electrolysis of 1mM of **1'$(OH_2)^{2+}$**) at –1.2 V vs. Ag/AgCl (0.1 M KBr) of an aqueous solution with (orange) and without (blue) phosphate buffer at pH = 7.

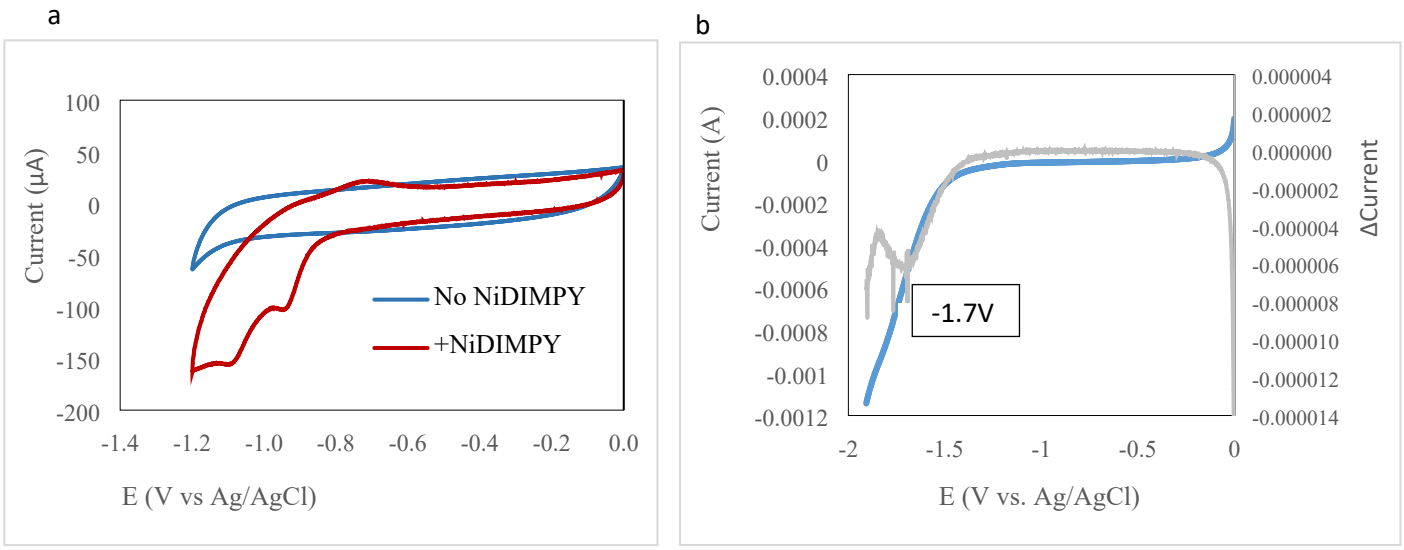

Figure S14. A comparison of cyclic voltammograms with (red) and without (blue) **1'(OH$_2$)$^{2+}$** in 100mM KBr in 0.3M phosphate buffer pH=7. Measurements used a glassy carbon (GC) working electrode, Ag/AgCl reference electrode. b) LSV of a solution in the absence of **1'(OH$_2$)$^{2+}$**). The gray markers represent application of the method of first principles to the blue curve. Minima denote inflection points in the catalytic curve and indicate the associated onset potential and current enhancement at the GC electrode.

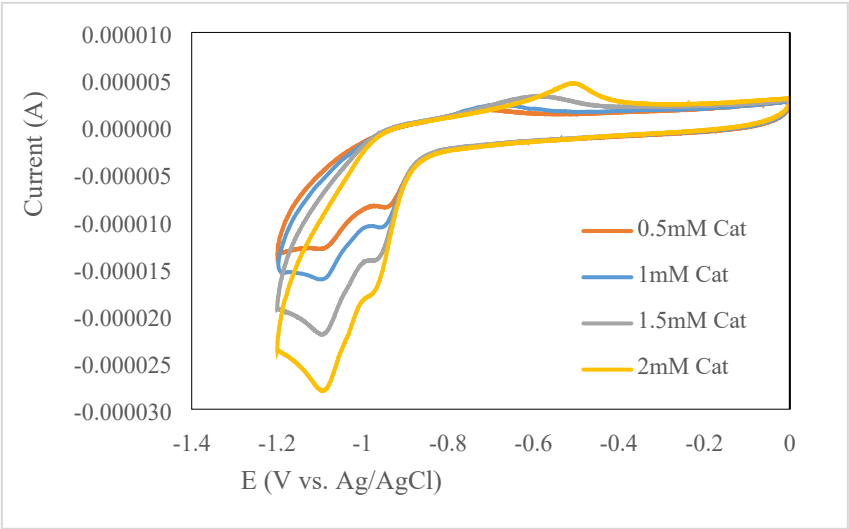

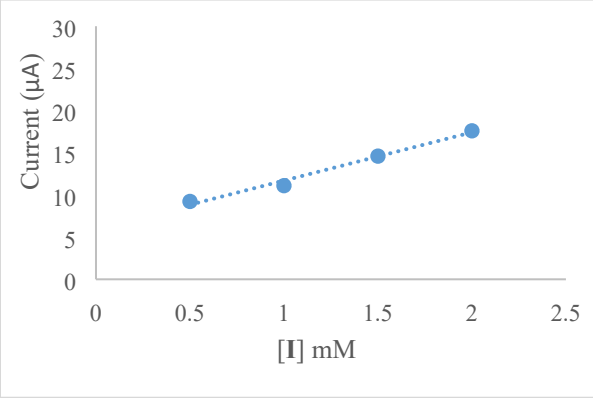

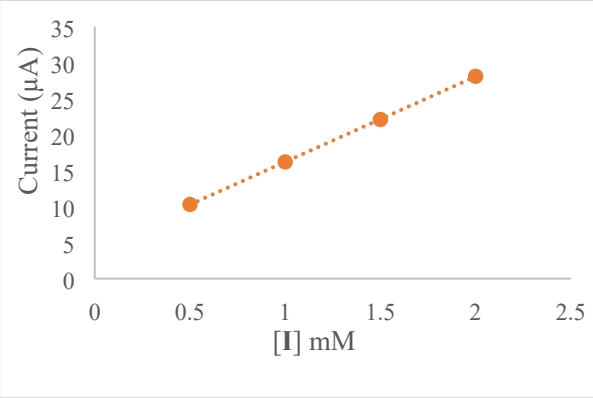

Figure S15. a) Cyclic voltammogram in presence of different concentration of complex [Ni(κ^3-2,6-{PhNCMe}$_2$(NC$_5$H$_3$)(OH$_2$)]$^{2+}$ (**1'(OH$_2$)$^{2+}$**) with 100mM KBr in 0.3M phosphate buffer pH=7, using a glassy carbon (GC) working electrode, Ag/AgCl reference electrode. Dependence of current to the concentration of **1'(OH$_2$)$^{2+}$** at the b) first reduction and at the c) second reduction.

Table S6. Summary of data collected from CPE experiment.

Entry	[cat]	E (V vs. Ag/AgCl)	time (h)	solution	µmol H2	FE (%)
1	1 mM	-1.1V	2	No Buffer	4.43	89
2	0.5 mM	-1.1V	2	0.3M Phosphate Buffer	34.74	76
3	1 mM	-1.1V	2	0.3M Phosphate Buffer	45.43	96
4	1 mM	-1.1V	18	0.3M Phosphate Buffer	415	28
5	1 mM	-1.0V	2	0.3M Phosphate Buffer	2	63
6	1 mM	-1.2V	2	0.3M Phosphate Buffer	110	78

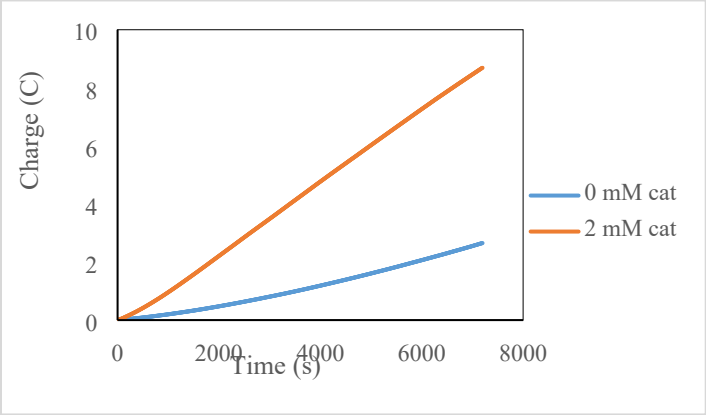

Figure S16. Controlled potential electrolysis at –1.2 V vs. Ag/AgCl (0.1 M KBr, phosphate buffer pH7) of an aqueous solution with **1'$(OH_2)^{2+}$** (orange) and without catalyst (blue).

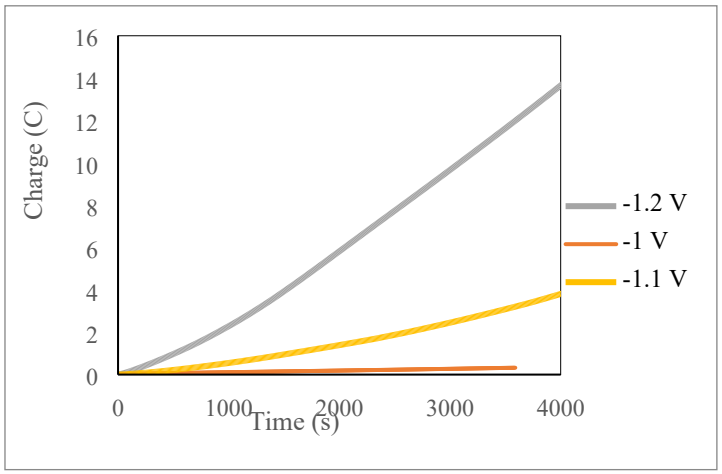

Figure S17. Controlled potential electrolysis of 1mM **1'$(OH_2)^{2+}$**) (0.1 M KBr, phosphate buffer pH = 7) at different potentials at vs. Ag/AgCl.

a

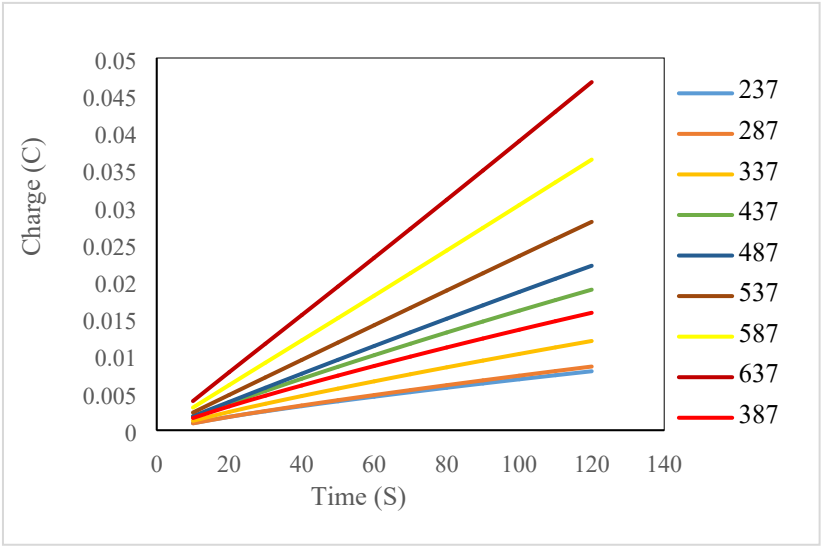

b

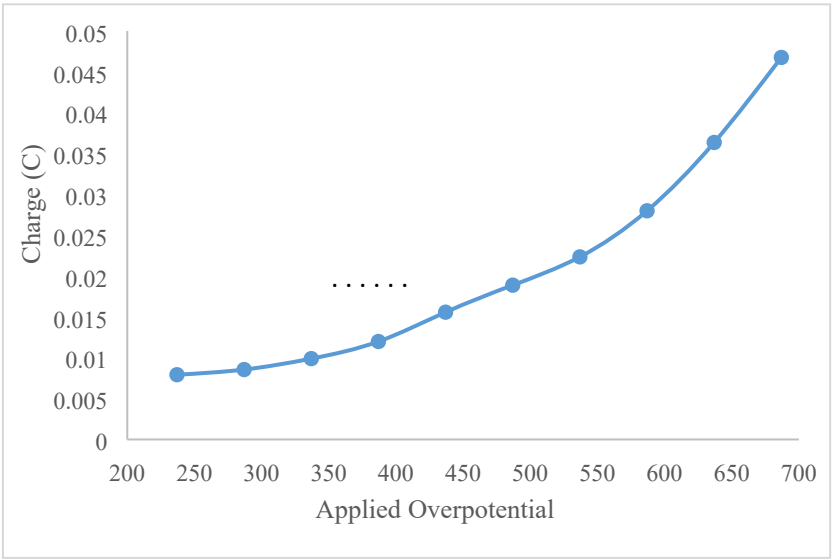

Figure S18. Using value of $E^{0}_{H^{+}/H_2}$ = 0.613 mV versus. Ag/AgCl for water at pH=7. a) Charge build up versus times and (b) the accumulated charge for controlled potential electrolysis of 0.5 mM solution of **1'(OH$_2$)$^{2+}$**) in 0.1 M KBr and phosphare buffer pH=7. The enhancement starts from overpotential=0.387 V

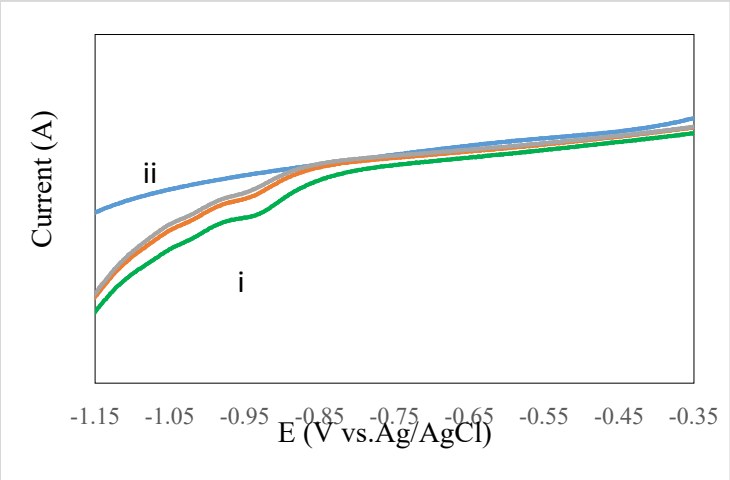

Figure S19. Linear Sweep Voltammetry measurements used to demonstrate that the working electrode surface remains clean during catalysis. Scans are shown for **1'$(OH_2)^{2+}$** (i) shows repeated linear scans of a solution containing 1 mM of **1'$(OH_2)^{2+}$**) complex in 0.1M KBr in phosphate buffered solution. (ii)Shows a scan after the electrode was removed, rinsed with clean solvent and placed in a fresh solution containing no Ni complex.

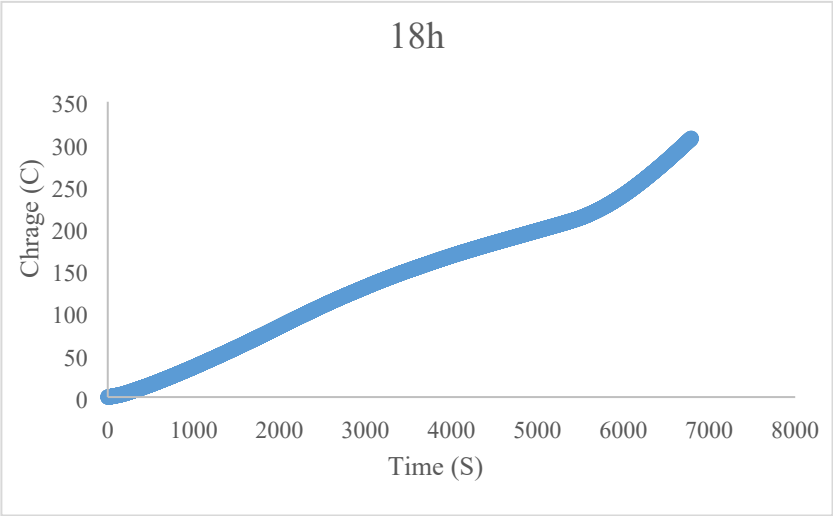

Figure S20. An 18 hour controlled potential electrolysis, demonstrating catalyst stability, of 1mM **1'$(OH_2)^{2+}$**) at –1.2 V vs. Ag/AgCl (0.1 M KBr, phosphate buffer pH=7).

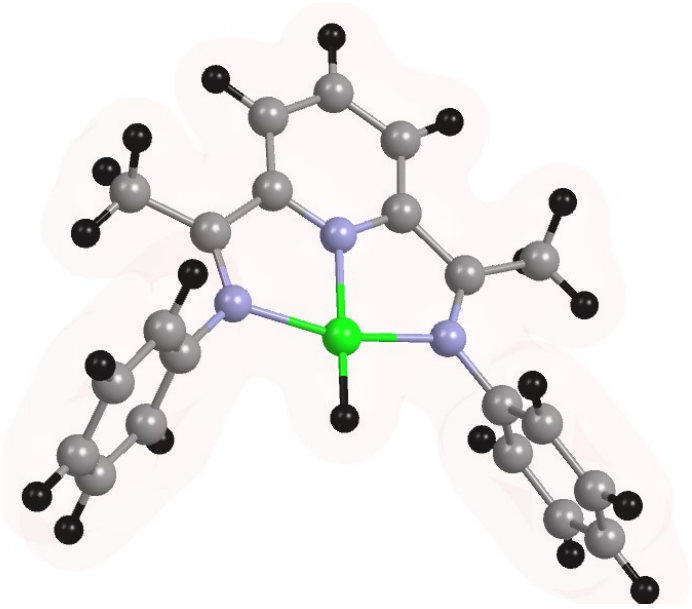

Figure S21. The structure obtained for the optimization of $[Ni(\kappa^3\text{-}2,6\text{-}\{PhNCMe\}_2NC_5H_3)(H)]^+$ (**Ni(II)H**), Obtained using the B3LYP functional, def2TZVP basis set and PCM model for solvation in water. This species was obtained after the protonation of $[Ni(\kappa^3\text{-}2,6\text{-}\{PhNCMe\}_2(NC_5H_3)(OH_2)]^{2+}$ as described in the text.

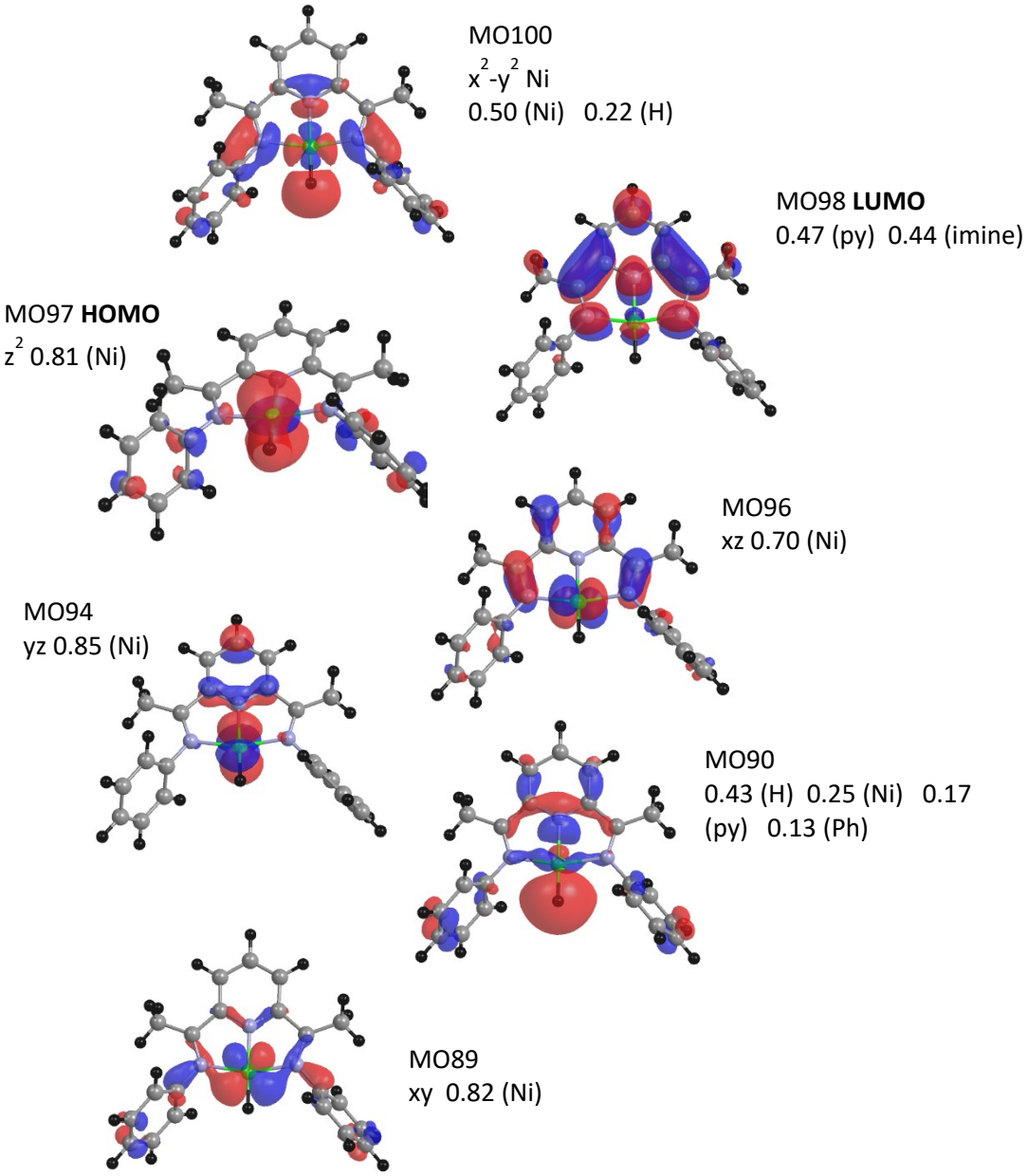

Figure S22. Selected molecular orbitals, focusing on the Ni d orbitals, obtained for the optimization of [Ni(κ^3-2,6-{PhNCMe}$_2$NC$_5$H$_3$)(H)]$^+$ (**Ni(II)H**), Obtained using the B3LYP functional, def2TZVP basis set and PCM model for solvation in water. Major fragment orbital contributions were visualized using the Chemissian program using a 0.03 isosurface.

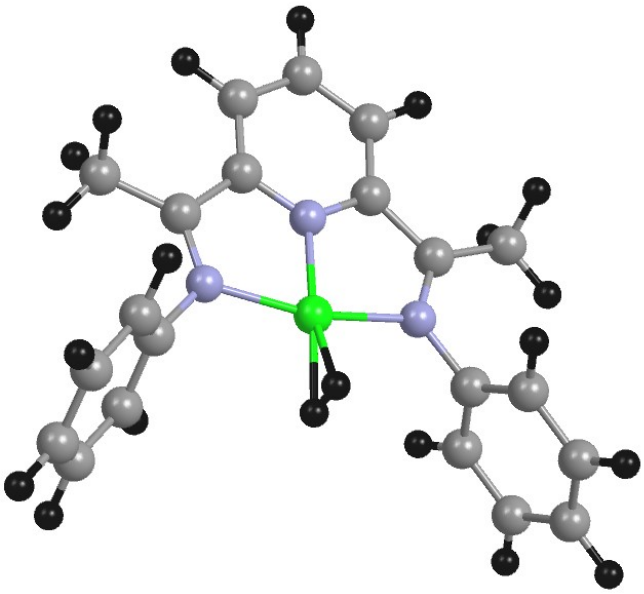

Figure S23. The structure obtained for the optimization of $[Ni(\kappa^3\text{-}2,6\text{-}\{PhNCMe\}_2NC_5H_3)(H_2)]^{2+}$ (**Ni(II)(H)$_2$**). Obtained using the B3LYP functional, def2TZVP basis set and PCM model for solvation in water. This species was obtained after the protonation of $[Ni(\kappa^3\text{-}2,6\text{-}\{PhNCMe\}_2(NC_5H_3)H]^+$ as described in the text.

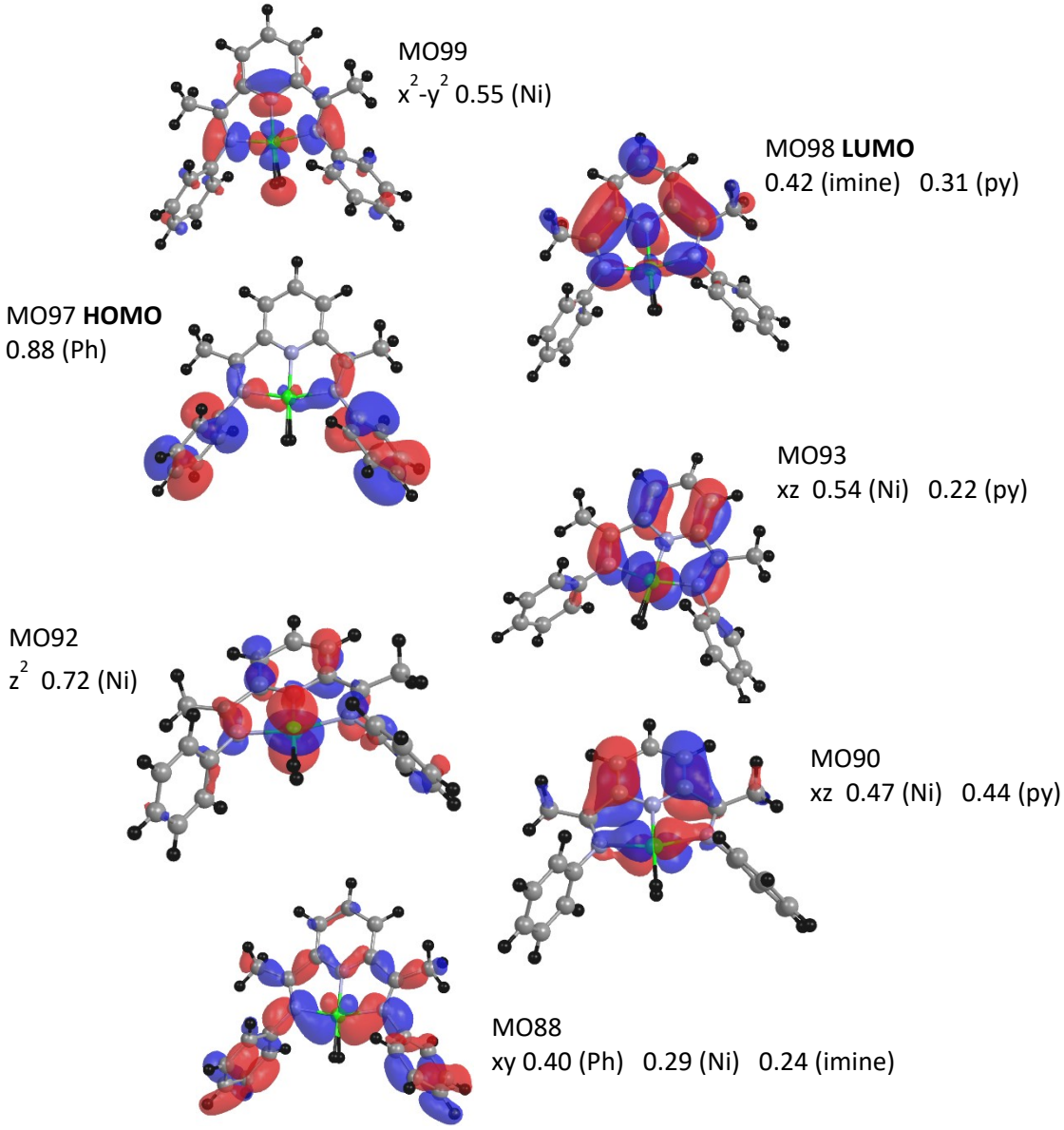

Figure S24. Selected molecular orbitals, focusing on the Ni d orbitals, obtained for the optimization of [Ni(κ^3-2,6-{PhNCMe}$_2$NC$_5$H$_3$)(H$_2$)]$^{2+}$ (**Ni(II)(H)$_2$**. Obtained using the B3LYP functional, def2TZVP basis set and PCM model for solvation in water. Major fragment orbital contributions were visualized using the Chemissian program using a 0.03 isosurface.

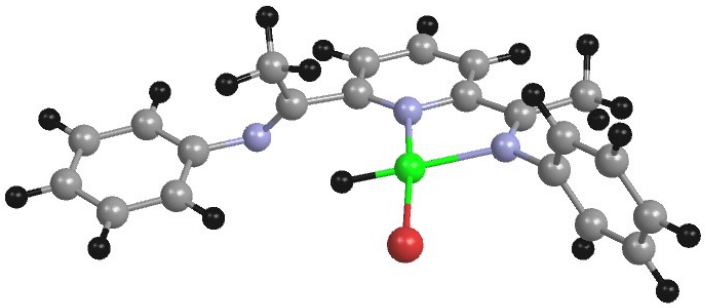

Figure S25. The structure obtained for the optimization of $[Ni(\kappa^2\text{-}2,6\text{-}\{PhNCMe\}_2NC_5H_3)(H)Br]^+$ (**Ni(II)BrH**), Obtained using the B3LYP functional, def2TZVP basis set and PCM model for solvation in acetonitrile. This species was obtained after the protonation of $[Ni(\kappa^3\text{-}2,6\text{-}\{PhNCMe\}_2(NC_5H_3)Br]^+$ (**1'**$^+$) as described in the text.

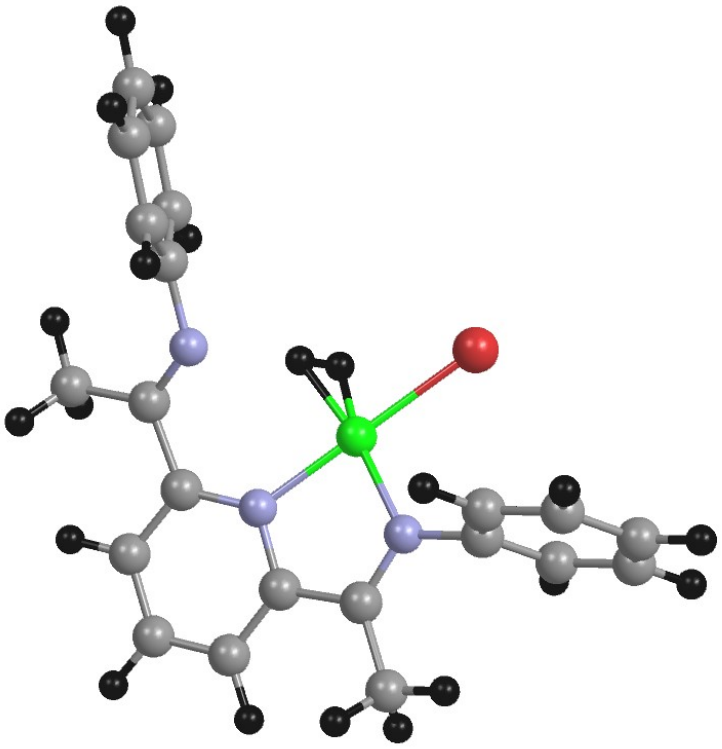

Figure S26. The structure obtained for the optimization of $[Ni(\kappa^2\text{-}2,6\text{-}\{PhNCMe\}_2NC_5H_3)Br(H_2)]^+$ (**Ni(II)Br(H_2)**), Obtained using the B3LYP functional, def2TZVP basis set and PCM model for solvation in acetonitrile. This species was obtained after the protonation of $[Ni(\kappa^2\text{-}2,6\text{-}\{PhNCMe\}_2NC_5H_3)(H)Br]^+$ (**Ni(II)BrH**), as described in the text.